frontiers | Frontiers in Physics

TYPE Original Research
PUBLISHED 05 January 2026
DOI 10.3389/fphy.2025.1712273

OPEN ACCESS

EDITED BY
Andrea Gonzalez-Montoro,
Polytechnic University of Valencia, Spain

REVIEWED BY
Rok Pestotnik,
Institut Jožef Stefan (IJS), Slovenia
Hadi Rezaei,
Shiraz University of Medical Sciences, Iran

*CORRESPONDENCE
Boris Vervenne,
boris.vervenne@ugent.be

†These authors have contributed equally to this work and share first authorship

RECEIVED 24 September 2025
REVISED 11 November 2025
ACCEPTED 14 November 2025
PUBLISHED 05 January 2026

CITATION
Dhaenens E, Vervenne B, Abi Akl M, Maebe J, Vanhove C and Vandenberghe S (2026) Simulation study of a low-cost Slide-Through PET scanner based on narrow flat panels with monolithic detectors.
Front. Phys. 13:1712273.
doi: 10.3389/fphy.2025.1712273

Simulation study of a low-cost Slide-Through PET scanner based on narrow flat panels with monolithic detectors

Elke Dhaenens†, Boris Vervenne*†, Maya Abi Akl, Jens Maebe, Christian Vanhove and Stefaan Vandenberghe

Department of Electronics and Information Systems, Medical Image and Signal Processing (MEDISIP), Ghent University, Ghent, Belgium

Background: Patient throughput in conventional PET systems is constrained by limited system sensitivity and the need for bed positioning. This study proposes a cost-effective Slide-Through PET (ST-PET) design based on two narrow monolithic LYSO detector panels with depth-of-interaction (DOI) readout. Each vertical panel has a length of 190.5 cm and consist of a 20.9-cm-wide top part for scanning the torso, and a 10.3-cm-wide bottom part to image the legs. The panels translate laterally relative to a standing patient to cover a 73.9 cm-wide field of view.

Methods: The ST-PET system was simulated in GATE and compared with two reference designs: a cylindrical PET system, and a wide static flat-panel PET. All systems used identical high-resolution monolithic LYSO detectors (300 ps time-of-flight, 2.67 mm DOI). Different panel motion strategies were explored for the ST-PET, and system performance was assessed in terms of sensitivity, spatial resolution, and image quality using NEMA image quality and anthropomorphic XCAT phantoms.

Results: Parallel motion of the panels ensured complete anatomical coverage, whereas other motion strategies provided focused but incomplete sampling. Sensitivity for a whole-body water phantom was 1.66 cps/kBq in the upper region and 0.52 cps/kBq in the lower region, whereas the cylindrical reference system provided 1.05 cps/kBq in both regions. The ST-PET system achieved sub-3 mm spatial resolution in the center of the field of view. Image quality varied between the upper and lower ST-PET sections, with superior contrast recovery and noise characteristics in the torso region. Shorter scan times suffice using the ST-PET to obtain similar noise characteristics in the lung and liver than with the cylindrical reference. Mild elongation artifacts are observed in the IQ and XCAT images for both flat-panel systems.

Conclusion: ST-PET demonstrates the feasibility of a compact sliding-panel geometry that delivers high spatial resolution and competitive sensitivity while enabling workflow efficiencies that could enhance throughput in clinical PET. Additional improvements in TOF resolution are needed to mitigate limited

angle artifacts, which would further enhance the relevance of such a narrow-panel geometry.

KEYWORDS

flat-panel detectors, Monte Carlo simulation, performance evaluation, high-throughput imaging, cost-efficient imaging, non-conventional geometries, upright imaging, time-of-flight

1 Introduction

Recent advancements in positron emission tomography (PET) technology have enabled the construction of long axial field of view (LAFOV) PET systems, and a number of (commercial) devices has become available over the past years: the uEXPLORER (194 cm [1]), the Siemens Biograph Vision Quadra (106 cm [2]), the PennPET Explorer (142 cm [3]), the GE Omni (32 cm, extendable up to 128 cm [4]), and the United Panorama (148 cm [5]). Compared to standard axial field of view (SAFOV) PET systems, these provide sensitivity gains with a factor 10–40 for body scans, enabling faster scan times, lower tracer doses, and improved image quality [6]. The extended AFOV however comes with several challenges, spurring research into alternative detector technologies and system geometries. One common limitation of the listed systems is that they are unable of estimating the depth of interaction (DOI), while this information is essential to avoid mispositioning of oblique lines-of-response (LORs). As a result, these systems are susceptible to parallax errors towards larger radial offsets, where the gamma photons are more likely to reach the detector surface at an oblique angle. This leads to non-uniform resolution losses and blurring effects. Since more oblique LORs are measured in LAFOV PET, this implies an increase in parallax-related spatial uncertainties [7]. To counteract these effects, the Advanced Molecular Imaging Team at Shenzen Bay Laboratory is developing a next-generation LAFOV ($>$ 1.4 m) PET system that incorporates DOI-capable detectors [8]. Similarly, the semi-monolithic LAFOV IMAS system under construction at the University of Valencia aims for homogeneous sub-4 mm spatial resolution throughout the full FOV [9] by incorporating DOI information.

Another system based on DOI-capable detectors is proposed by the MEDISIP group at Ghent University, which aims to solve an additional important challenge: the high cost of LAFOV PET. In this Walk-Through PET (WT-PET), the detectors are arranged into two opposing vertical panels ($71\times$ $106\,\mathrm{cm}^2$) instead of the standard cylindrical shape. The use of monolithic lutetium-yttrium oxyorthosilicate (LYSO) detectors ($50\times$ $50\times 16\,\mathrm{mm}^3$) not only provides high spatial resolution across the field of view, but also allows detector spacing as close as 50 cm, boosting the geometric sensitivity of the system. These detectors, namely, infer the DOI from measurements of the light spread across multiple silicon photomultipliers (SiPMs); consequently, the oblique LORs associated with close detector spacing are correctly localized and do not lead to parallax blurring. Monte Carlo simulations have demonstrated that the WT-PET system provides comparable sensitivity to high-end systems like the Biograph Vision Quadra [10], but at a significantly lower component cost. Despite the presence of mild elongation artifacts in the images due to the missing projections in the direction of the gaps, images of sufficient quality can be obtained with good contrast recovery of small lesions. Additionally, the design allows high throughput by upright imaging and autonomous patient positioning, significantly reducing scan times compared to cylindrical PET systems. As such, the system represents a cost-effective alternative to current commercially available devices [11].

Building upon this concept, the present work proposes a new Slide-Through PET (ST-PET) system, which aims for a similar number of detectors (and thus cost) as a conventional SAFOV PET, while significantly accelerating patient throughput. Like the WT-PET, the design consists of two opposing vertical detector panels with the same monolithic DOI-capable LYSO scintillators. The detectors are however rearranged so that they cover the entire length of the patient. To reduce the cost, the panels are made much narrower, and split into a torso and leg part - respectively 4 and 2 detectors wide, resulting in dimensions of $105.7\times 20.9\,\mathrm{cm}^2$, and $84.5\,\mathrm{cm}\times 10.3\,\mathrm{cm}^2$. This layout provides higher sensitivity at the torso and head region where it is most clinically relevant, and accounts for the fact that the legs attenuate the signal less strongly than the body. To cover the entire anatomy, the panels move laterally with respect to the patient over a range of 73.9 cm as shown in Figure 1.

One important challenge of dual-flat panel system geometries, including the WT-PET, is their limited angular coverage, which introduces characteristic elongation artifacts towards the panels in the reconstructed images. Measurement of time-of-flight (TOF) information however counteracts these effects, as it relaxes the requirements for complete angular sampling [12, 13]. Simulations of the WT-PET showed that a TOF resolution of 300 ps already strongly reduces their presence, but some other groups working on dual flat-panel configurations aim for even lower TOF resolutions to fully eliminate limited angle effects, such as the sub-100-ps dual panel PET system proposed by Razdevšek et al. [14]. An important open question for this very narrow system geometry is thus whether current TOF resolutions provide sufficient performance and image quality, or whether even better timing capabilities are needed. Additionally, different panel motion strategies provide distinct sensitivity distributions and angular coverage, and investigations are needed to determine the optimal motion pattern to image a standard adult patient.

2 Methods

First, a study was performed to determine the optimal panel motion strategy for the ST-PET. Subsequently, the characteristics of the system were investigated using phantom

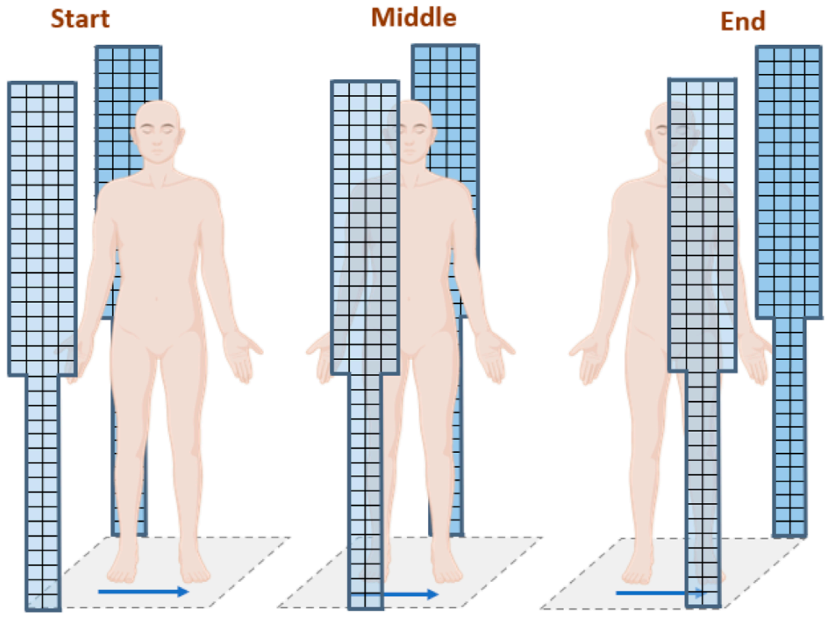

FIGURE 1
Design and scanning principle of the Slide-Through PET system. The two vertical detector panels are spaced 50 cm apart and move laterally over 73.9 cm with respect to the patient.

studies, based on the National Electrical Manufacturers Association (NEMA) standard but optimized and adjusted for the non-conventional system geometry [15]. To benchmark and explain the results, two reference systems–a wide flat-panel system and a cylindrical SAFOV PET–were simulated where relevant.

2.1 Simulation and reconstruction framework

All systems are based on the same monolithic detectors, consisting of a 50 × 50 × 16 mm^3 LYSO crystal coupled to an 8 × 8 array of 6 × 6 mm^2 SiPMs. The geometries are visualized in Figure 2 and were modeled in the Geant4 Application for Tomographic Emission (GATE) v9.4 [16] as follows. The `emstandard` physics list was used for all simulations.

(i) The ST-PET system features two vertical flat detector panels spaced 50 cm apart, each divided into an upper section (105.7 × 20.9 cm^2) for torso and head imaging, and a narrower lower section (84.5 × 10.3 cm^2) for the legs. The system comprises a total of 224 detector modules arranged with a 53 mm pitch. The patient stands upright on a platform that moves relative to the panels. The total lateral coverage for the upper section of the panels was 73.9 cm, and the coincidence time window (CTW) was set to 6.6 ns, calculated from the longest diagonal distance present in the geometry. The CTW of the other systems was calculated analogously.

(ii) The ReferenceFP system uses two wide opposing detector panels (190.5 × 73.9 cm^2 each) spaced 50 cm apart, fully covering the standing patient without any motion. It incorporates 1008 detector modules arranged with a 53 mm pitch. The CTW was set to 7.0 ns. This configuration, which covers a much wider solid angle, was included to analyze the impact of constraining the transverse dimensions.

(iii) The ReferenceCYL system consists of a similar number of detectors (225) as the ST-PET, but now arranged in a cylindrical geometry. The system features a full 80 cm diameter detector ring with an axial pitch of 52 mm to cover a 25.8 cm axial field of view (AFOV), similar to the Siemens Biograph Vision 600 [17]. The patient lies on a bed, which translates axially to cover 190.5 cm. The CTW was set to 3.0 ns.

The spatial and time resolutions of the detectors were modeled post-simulation by applying a Gaussian kernel to the exact interaction positions and times obtained from GATE [10]. Values for the detector resolution were adopted from Stockhoff et al. [18], who obtained an in-plane spatial resolution of 1.14 mm full width at half maximum (FWHM) and DOI resolution of 2.67 mm FWHM for this detector configuration. The TOF was set to 300 ps as in our other simulation models [19], estimated from values reported in literature for similar monolithic detectors [20–22].

List-mode data containing only true coincidence events were used for image reconstruction. Reconstruction was performed using the maximum likelihood expectation maximization (MLEM) algorithm without subsets as implemented in PETRecon, an in-house reconstruction package developed in Julia [23]. All reconstructions used voxel sizes of 2 × 2 × 2 mm^3, except the spatial resolution study, for which a small voxel size of 0.25 × 0.25 × 0.25 mm^3 was used. Normalization correction was implemented as described in [24] to account for the systems' non-uniform geometric sensitivity and detector attenuation effects. Additionally, attenuation correction using the ground truth attenuation map was applied for all reconstructions.

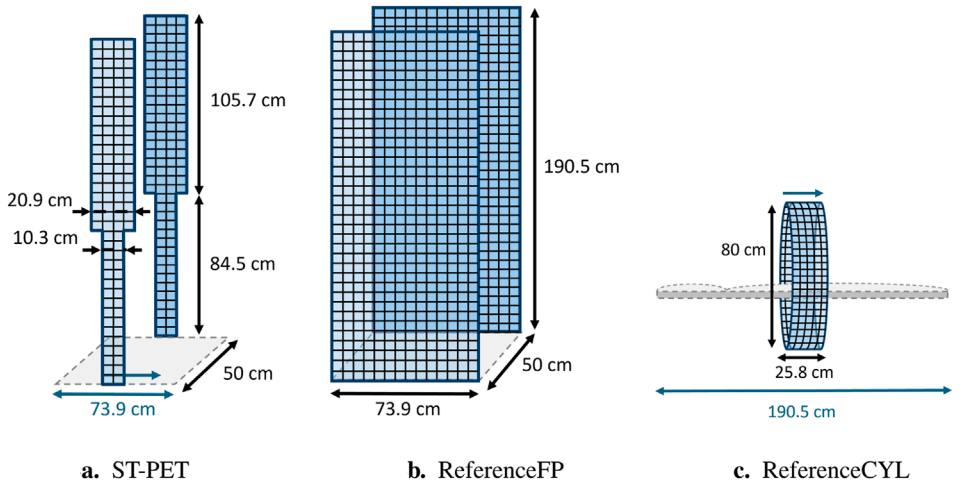

FIGURE 2
System geometries of **(a)** the Slide-Through PET, **(b)** the large flat-panel reference design, and **(c)** the cylindrical reference design. Blue arrows indicate the range of motion.

2.2 Phantom studies

2.2.1 ST-PET panel motion strategies

Three different motion strategies were considered for scanning, as shown in Figure 3: (i) parallel motion, where both panels translate laterally in the same direction; (ii) opposite motion where panels move simultaneously in opposite lateral directions; and (iii) single panel motion, where one panel remains static at the center while the other moves laterally over the full range. To investigate the sensitivity across the FOV for these different strategies, a uniform box source ($73.9 \times 50.0 \times 190.5$ cm^3) containing 1 MBq of homogeneous activity was placed between the panels of the ST-PET and simulated for 20 min using back-to-back gamma photons. No surrounding medium was added, in order to obtain an attenuation-free measure of sensitivity throughout the field of view (FOV). The emission positions of the detected coincidences were binned into a 3D histogram over the full FOV, and spatial count distributions were visualized on a coarse $10 \times 10 \times 10$ mm^3 grid to ensure sufficient statistics.

To investigate the differences in angular sampling completeness for each of the different motion strategies, sinograms were computed that show which LORs theoretically can and cannot be measured in the transverse plane. This was done by sampling the Cartesian coordinates (x, y) of all possible LORs between the detector panels and converting them into radial coordinates (r, θ). To contextualize these findings with respect to the dimensions of a standard patient, the resulting binary masks were overlaid over the sinogram of an abdominal slice of an anthropomorphic Extended Cardio Torso (XCAT) phantom with standard body mass index (BMI).

2.2.2 Sensitivity

To study the intrinsic sensitivity of the systems in a stationary condition, 1-mm-diameter line sources with a length of respectively 70 cm and 190 cm were positioned along the scanner axes. These contained 1 MBq activity of a back-to-back gamma photon source. No attenuating medium was added to the measurement so that the attenuation-free sensitivity was obtained directly from the ratio between the number of detected true counts and the total simulated activity. This methodology eliminates the need for the NEMA interpolation method based on aluminum sleeves to obtain the attenuation-free measurement. The 70 cm line source was used to benchmark the sensitivity of the ReferenceCYL system against reported values for the Siemens Biograph Vision 600 [17], while the 190 cm line source was used to compare sensitivity between the ST-PET and ReferenceFP systems. These different simulations are visualized in Figure 4. All line source simulations were performed with stationary systems. For the ReferenceCYL system, this was done to enable comparison with reported NEMA measurements of the Biograph Vision 600, which were performed without axial translation. For the comparison of the ST-PET and ReferenceFP, a stationary acquisition was used to assess how differences in transverse solid angle impact the sensitivity values.

Additionally, a 190-cm-long cylindrical phantom with 20-cm-diameter was filled with water and 1 MBq of back-to-back gamma photons and positioned along the scanner axis as a more clinically relevant measure of the sensitivity for a whole-body scan with attenuation. The whole-body scanning protocol was then used to measure the sensitivity of the ST-PET and referenceCYL; this means that a 73.9 cm lateral motion was performed for the ST-PET, while the cylindrical reference system covered a total axial range of 190.5 cm. This study is depicted in Figure 4 as well. The dynamic scanning mode was used for both the ST-PET (lateral translation) and ReferenceCYL (axial translation) so that the acquisition protocol corresponds to the one that would be used in clinical practice for a whole-body scan. The overall sensitivity was again calculated by dividing the total number of true counts with the total number of emissions. To visualize axial variations in detection efficiency, axial sensitivity profiles were calculated for both systems by counting the number of true coincidence events per 2-mm-thick axial slice. This number was then normalized by the total source activity and the simulation time.

For the ST-PET, separate sensitivity values are included for the top and bottom panel besides the "full phantom" value to allow for a

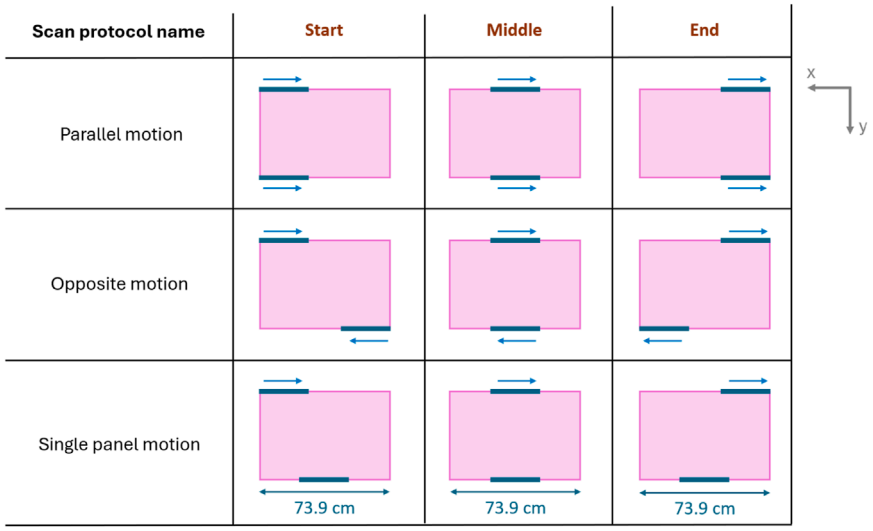

FIGURE 3
Illustration of the three panel motion strategies investigated for the Slide-Through PET system.: (i) parallel motion, (ii) opposite motion, (iii) single panel motion.

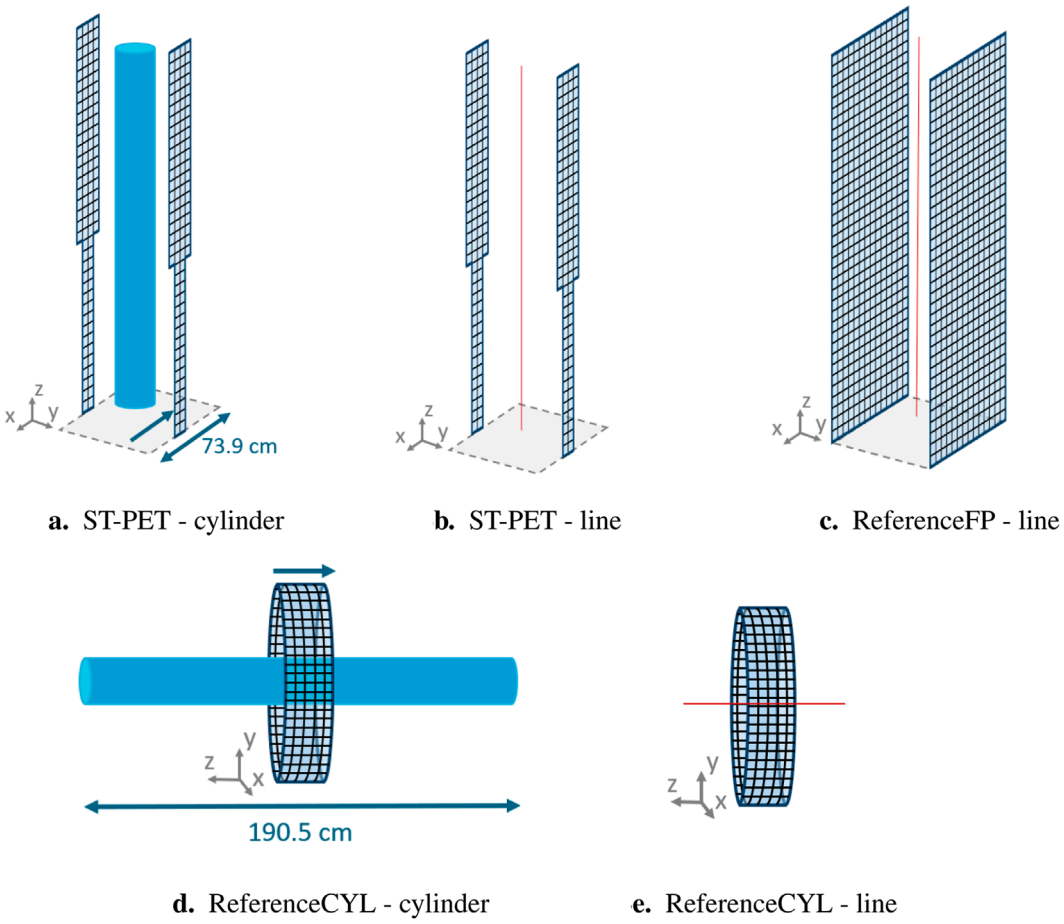

FIGURE 4
Overview of sensitivity simulation setups. All systems were stationary, except in **(a)** and **(d)** where motion (indicated in blue) was used to cover the full extent of the 190 cm cylindrical water phantom. **(b)** and **(c)** show the placement of the 190 cm line source at the center of the scanner, while **(e)** shows the placement of the 70 cm line source.

more fine-grained analysis of the difference in sensitivity between the different sections. These values were obtained by splitting the emitted activity and detected counts into the separate sections, and calculating the ratio for the two regions independently.

2.2.3 Spatial resolution

The spatial resolution was only evaluated for the ST-PET system. To this end, three 0.5-mm-diameter ^{18}F point sources were placed as shown in Table 2: the first one centrally between the top panels, the second one with a 10 cm offset towards one of the panels, and the last one 40 cm axially above center. While the NEMA protocol mandates the use of Filtered Backprojection, it results in strong image artifacts for data with truncated angular coverage. To obtain a more representative measure of resolution performance, MLEM was used instead to reconstruct the point data. Since iterative methods can artificially enhance the resolution in the absence of a warm background [25], each point source was embedded in a 15-mm-diameter cylindrical warm water phantom with a length of 30 mm. These were oriented towards the detector panels, i.e., along the direction that is affected by elongation artifacts due to limited angular coverage. The background activity was set to 1.230 MBq, and the source-to-background activity concentration ratio was set to 134:1. The latter was downsampled post-simulation to obtain a reconstructed source-to-background contrast of approximately 1.3:1, which is sufficiently low to avoid overestimation effects [19]. This reconstructed point source contrast was defined as the ratio of the reconstructed point peak intensity (peak + background) to the background intensity. Data were acquired with the stationary ST-PET system and at least 100,000 true coincidence events were obtained per source position. The 15th iteration was used to ensure convergence of the measurements. Following the methodology described in [19], two reconstructions were generated per source to facilitate the evaluation: a background-only image and a full image of the point source and background. By subtracting these images, a source-only image was obtained, from which line profiles were extracted to quantify the FWHM in the x-direction (parallel to the panels), y-direction (perpendicular to the panels) and z-direction (along the scanner's central axis).

2.2.4 NEMA image quality

To assess the contrast and noise characteristics of the ST-PET, the NEMA image quality (IQ) phantom with six hot spheres (diameters: 10, 13, 17, 22, 28, and 37 mm) and a central lung insert was simulated. The phantom's uniform background activity concentration was kept constant at 5.3 kBq/mL, while three different (4:1, 3:1, 2.5:1) sphere-to-background activity concentration ratios were studied. The phantom was positioned at the center of the FOV of both the upper and lower panel sections of the ST-PET system, and a lateral translation over a 73.9-cm-range was performed as illustrated in Figure 5. A 4-min scan time was used and non-isotropic point spread function (PSF) modeling was applied during image reconstruction using a (1.3, 2.5, 1.3) mm FWHM Gaussian kernel.

Images were obtained for 1–10 iterations of MLEM, and the contrast-to-noise ratio (CNR) and contrast recovery coefficient (CRC) were calculated at every iteration. To compute the CNRs and CRCs, the regions-of-interest (ROIs) were defined according to the

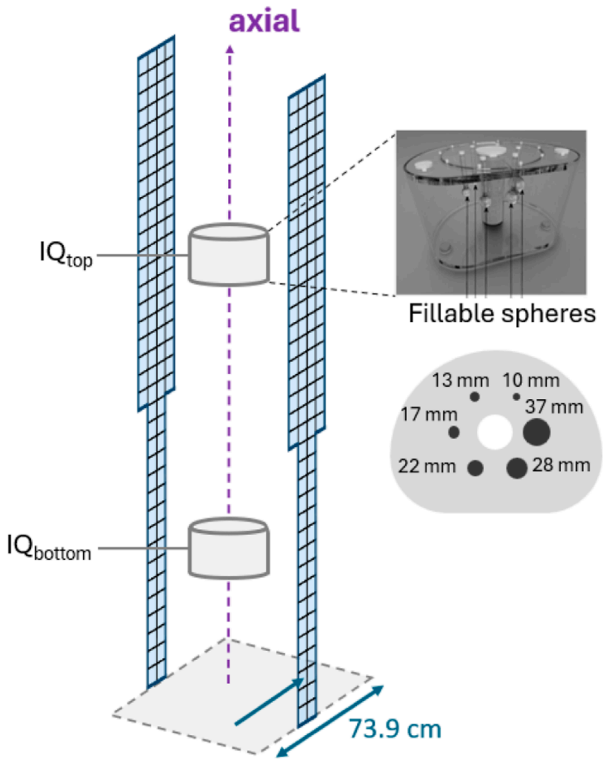

FIGURE 5
IQ phantom positions IQ_{top} and IQ_{bottom} within the ST-PET system.

NEMA standard. The CNR for hot sphere j was calculated according to Formula 1.

$$\mathrm{CNR}_j = \frac{C_{H,j} - C_{B,j}}{\mathrm{SD}_{B,j}}, \tag{1}$$

where $C_{H,j}$ is the average counts in the ROI of hot sphere j, and $C_{B,j}$ and $\mathrm{SD}_{B,j}$ are the mean and standard deviation of the counts in the background ROIs. The CRC for each hot sphere j was calculated using Formula 2

$$\mathrm{CRC}_j = \frac{\left(C_{H,j}/C_{B,j}\right) - 1}{R - 1} \times 100\%, \tag{2}$$

where $C_{H,j}$ and $C_{B,j}$ denote the mean counts in the hot sphere and corresponding background ROIs, and R is the true activity concentration ratio between the sphere and background. Evaluation of the background variability (BV) was omitted since no scattered and random coincidences are included. Consequently, the BV would mainly reflect differences in statistical noise; these differences are evident from the sensitivity study, and its impact on lesion observability is shown by the CNR calculations.

2.2.5 XCAT image quality

To evaluate the scanner performance for a more clinically relevant situation, anthropomorphic male XCAT phantoms of normal and high BMI were simulated. Both phantoms had an activity of 2 MBq/kg and the uptake ratio between organs was refined to match population averages reported by Dias et al. in [26]. Implementation details are specified in *Supplement 1: XCAT source*

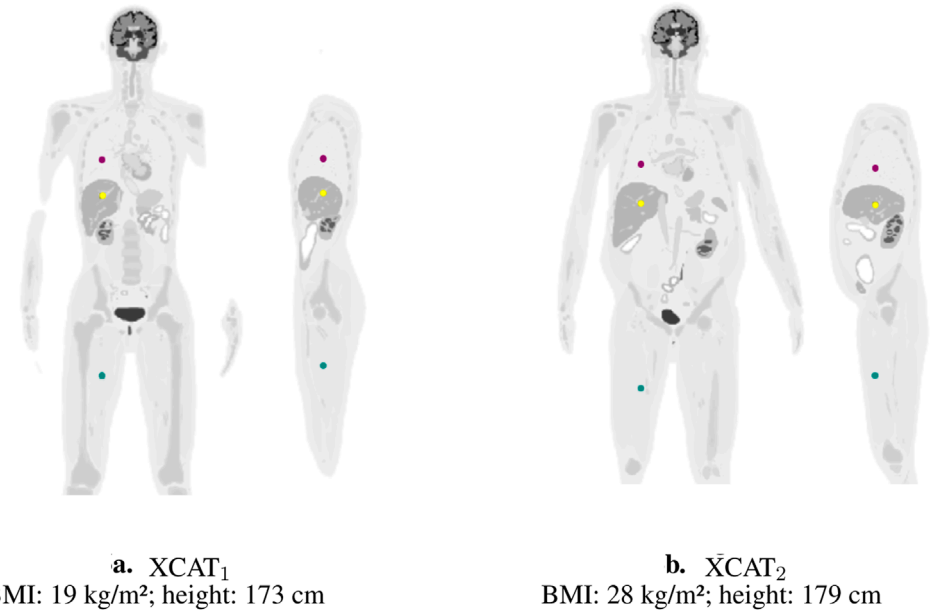

FIGURE 6
Visualization of the 13-mm-diameter spheres used for noise evaluation in the lung, liver, and leg spheres (purple, yellow, and blue respectively) for the central coronal and sagittal planes of **(a)** $XCAT_1$ and **(b)** $XCAT_2$.

distribution. Performance of the three systems was compared based on visual assessment and by quantifying the noise in three 13-mm-diameter ROIs. These were positioned in the lung, liver, and leg, as shown in Figure 6.

The first XCAT (BMI: 19 kg/m^2; height: 173 cm) was used to study how long each scanner needs to acquire data for in order to obtain images with similar noise characteristics. To this end, the acquisition time was varied between two and 10 minutes for the ST-PET and ReferenceCYL, and between 15 seconds to 1 minute for the ReferenceFP system. Afterwards, the standard deviation normalized with the mean was quantified as a noise metric and compared in the three ROIs, and scan times were determined that resulted in similar noise levels. The second XCAT (BMI: 28 kg/m^2; height: 179 cm) was then scanned for these fixed scan times, and the same ROI analysis was performed to investigate whether the same differences also hold true for a larger patient.

3 Results

3.1 ST-PET panel motion strategies

Figure 7 illustrates the spatial distribution of detected events for the three ST-PET motion strategies. The parallel panel motion homogeneously spreads out the sensitivity over the entire FOV, whereas the opposite and single panel motion concentrate the counts more effectively in certain regions of the FOV where the patient is positioned. However, the opposite motion and–especially for large patients–the single panel motion result in regions with very low to zero sensitivity, making imaging in those areas very challenging to impossible.

The static sinograms shown in Figure 8 highlight how the already limited angular coverage of the ReferenceFP system is further truncated by the narrow-panel design of the ST-PET. Broader coverage can be obtained by moving the panels, but the total extent remains limited within the bounds of the ReferenceFP since motion is laterally constrained within the dimensions of the ReferenceFP (73.9 cm). More specifically, the parallel panel movement results in equal but (strongly) truncated angular coverage over all relevant radial coordinates. Single panel motion covers a wider total range of angles, but the angular range covered by the detectors at each individual radial coordinate remains strongly truncated. Additionally, the total radial extent covered by the panels is reduced, causing larger patients to fall outside of the effective FOV. For instance, part of the arms are not covered by the panels for the displayed abdominal XCAT slice. Finally, the opposite panel motion provides much broader angular coverage for small radial coordinates, but no data are sampled at all beyond a radial offset of about 10 cm and 5 cm respectively (corresponding to half the width of the top and bottom panel). This makes this motion strategy unsuitable for imaging most patients, whose diameters generally measure over 20 cm. Based on these observations, the parallel motion is deemed the most optimal for full body imaging of adult patients, and is therefore used as the default in the remaining studies below.

3.2 Sensitivity

Table 1 summarizes the sensitivity measurements for the studied systems and phantoms. The sensitivity of the ReferenceCYL with the 70 cm line source closely matches that of the Vision 600, which shares a similar overall system design. For the 190 cm line source,

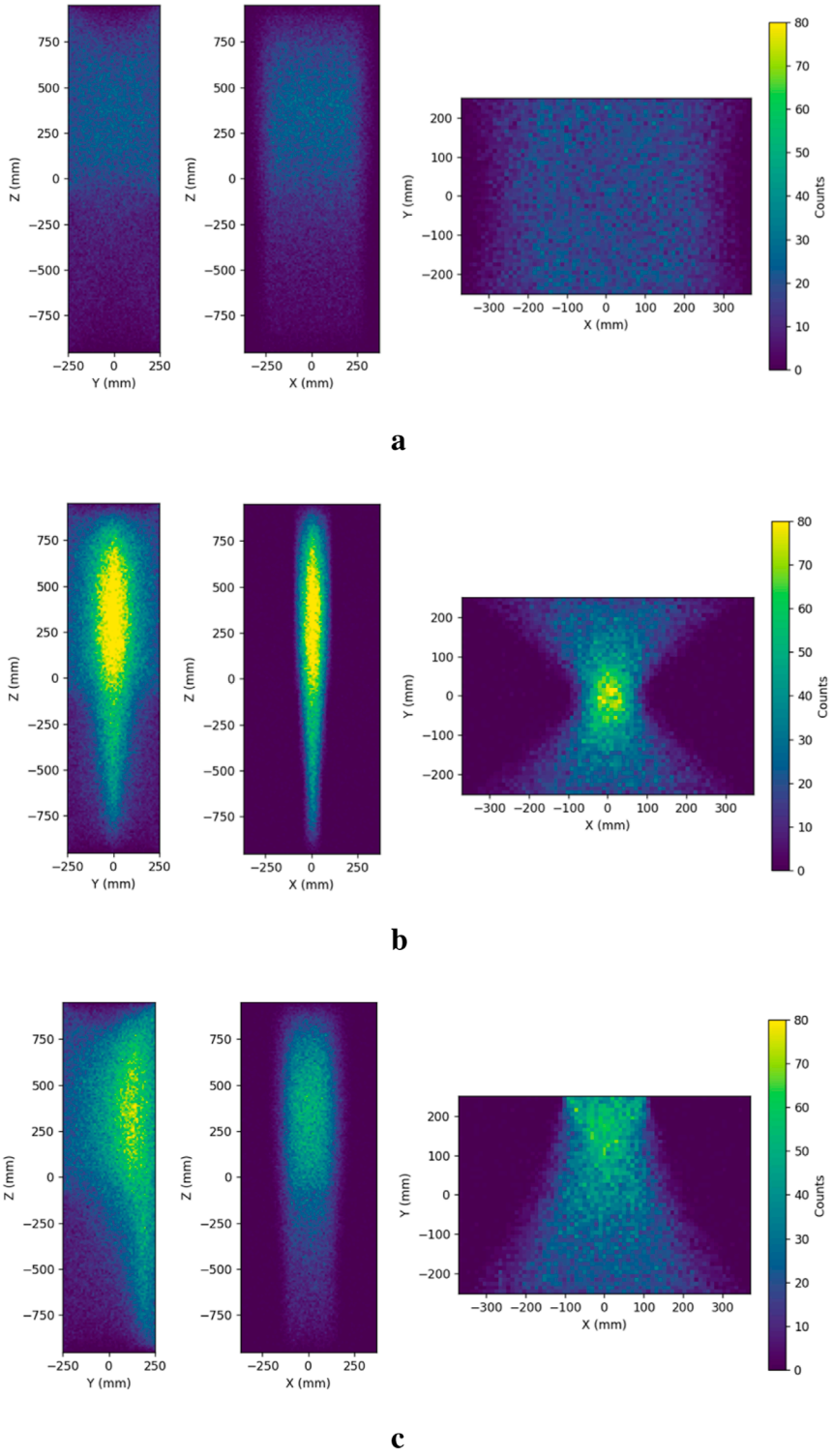

FIGURE 7
Histograms in the sagittal, coronal, and transverse views for the three simulated motion strategies on a 10 × 10 × 10 mm^3 grid. The three rows correspond to the three motion strategies: **(a)** parallel motion, **(b)** opposite motion, and **(c)** single panel motion.

the sensitivity of the ReferenceFP is about four times higher than the ST-PET, and the sensitivity in the top part of the ST-PET is almost double that of the bottom part.

For the 190 cm cylindrical phantom, even larger differences are observed between the two sections of the ST-PET, with the top panel providing three times the sensitivity of the bottom panel.

10.3389/fphy.2025.1712273

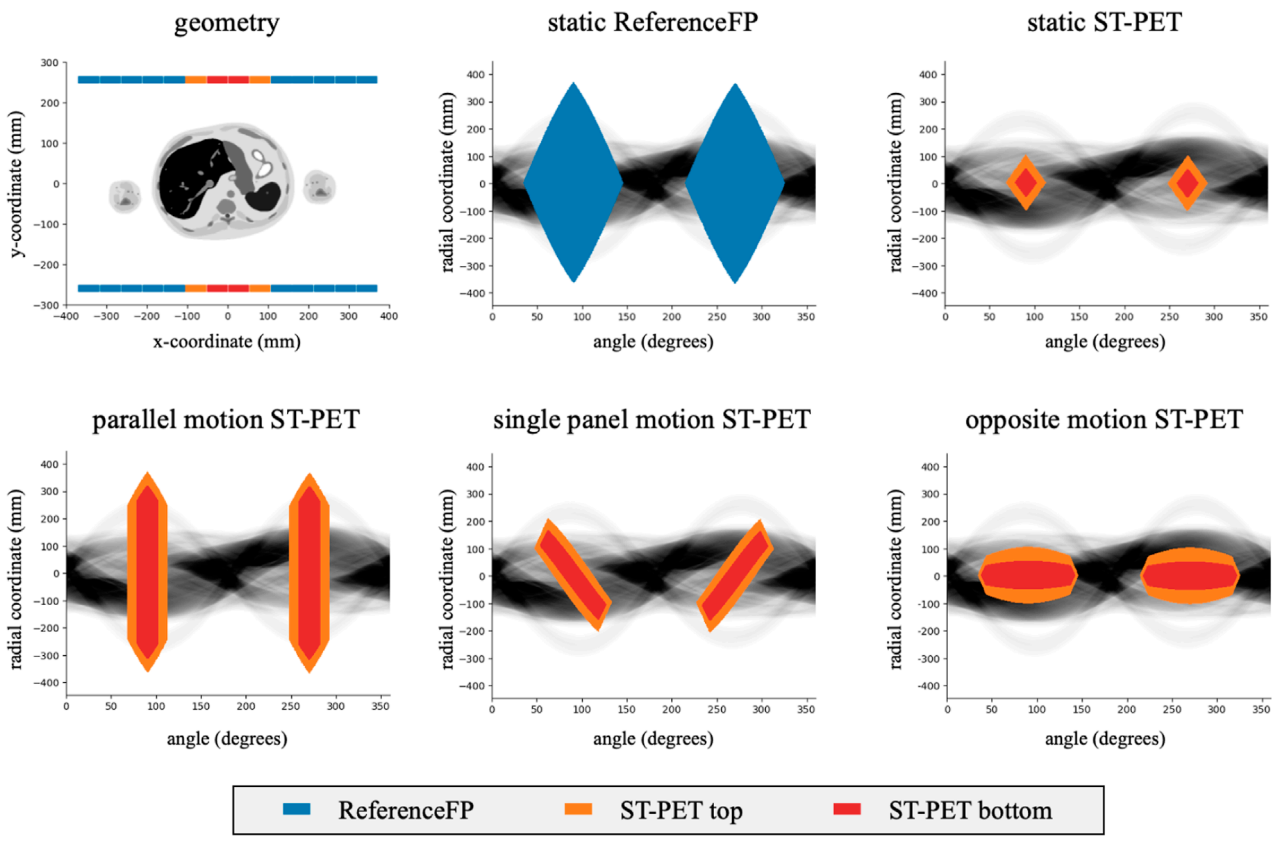

FIGURE 8
Sinogram representation of the data that can be sampled in the transverse plane for the different flat-panel configurations under study. The top row gives an overview of the geometries, and the calculated sinogram masks for the static ReferenceFP (blue) and ST-PET (orange and red, respectively for the top and bottom section). The bottom row displays how the data completeness is enhanced using different motion strategies. To give an idea of the dimensions of a standard patient, an abdominal slice of an XCAT phantom and the corresponding sinogram is included. However, it is important to note that the bottom part of the ST-PET is used to scan the legs, and would thus see a different anatomical structure.

TABLE 1 Sensitivity values for the performed measurements.

Scan condition	System	Sensitivity (cps/kBq)
70-cm-long line source (stationary)	ReferenceCYL	13.6
	Biograph Vision 600[a]	16.4
190-cm-long line source (stationary)	ST-PET (full phantom)	43.75
	ST-PET (top panel region)	54.82
	ST-PET (bottom panel region)	29.90
	ReferenceFP	162.03
20-cm-diameter, 190-cm-long cylindrical phantom (scanning motion)	ST-PET (full phantom)	1.16
	ST-PET (top panel region)	1.66
	ST-PET (bottom panel region)	0.52
	ReferenceCYL	1.05

[a]Experimental NEMA sensitivity value for Biograph Vision 600 obtained from literature [17].

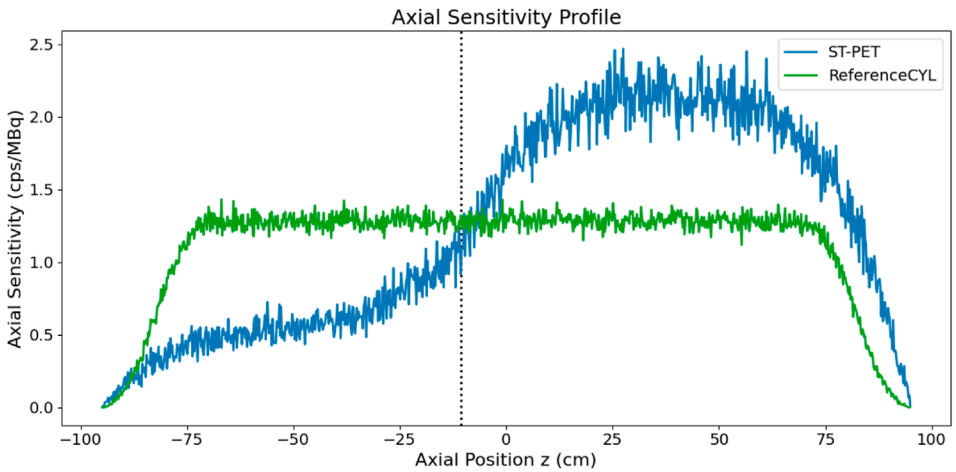

FIGURE 9
Axial sensitivity profiles for the moving ST-PET and ReferenceCYL systems, scanning the 190-cm-long cylindrical phantom with a diameter of 20 cm. The vertical black dotted line indicates the transition between top and bottom panel regions.

In this scenario, the overall sensitivity of the ST-PET is about 10% higher than that of the ReferenceCYL. The axial sensitivity profiles in Figure 9 clearly show that sensitivity along the axis of the ST-PET is non-homogeneous, as opposed to the referenceCYL system which provides a more or less constant value.

3.3 Spatial resolution

Table 2 presents the measured FWHM values for the ST-PET system at the three point source positions. The *x*-direction is parallel to the detector panels, the *y*-direction is perpendicular to the panels, and the *z*-direction aligns with the scanner's central axis. In general, the resolution is best in the center of the FOV with values well below 3 mm, and some deterioration occurs in the *y*-direction towards large axial offsets. The resolution in the *x* and *z* directions stays below 2 mm at all considered positions.

3.4 NEMA image quality

Figure 10 shows transverse slices of the reconstructed IQ images at iteration 5 for the two axial positions: IQ_{top} and IQ_{bottom}. Detected true count rates were 7.63 million counts/min for IQ_{top} and 2.03 million counts/min for IQ_{bottom} for the 4:1 contrast case. In both phantoms, elongation artifacts are visible in the direction towards the detector panels, particularly in the larger spheres and background. CNR values are larger for IQ_{top} compared to IQ_{bottom}, and the CNR drops significantly as the source-to-background ratio of the lesions is reduced. The maximum CNR is achieved in the second iteration for IQ_{top}, whereas there is no clear peak for IQ_{bottom}. Since the small spheres require some more iterations to reach good visibility, the fifth iteration is visualized, as it presents a good balance between image noise and contrast recovery. The CRCs increase with iteration for all sphere sizes and both positions. Generally, larger spheres show higher CRCs at each iteration, but all spheres are well-visible at the highest source-to-background ratio. Only at low contrast, the smallest sphere becomes hard to discern.

3.5 XCAT image quality

Figure 11 compares the noise levels in $XCAT_1$ for varying acquisition times. In the lung and liver, the ST-PET provides significantly lower noise levels at matched scan times than the ReferenceCYL system, while the noise in the legs is more or less the same. The ReferenceFP system shows significantly lower noise in all body regions, even for very short scan times. Based on the curves, a scan time of 4 min suffices for the ST-PET to obtain similar noise in the torso as a 9.15 min scan on the ReferenceCYL system, whereas the ReferenceFP system would only need 30 s.

Figure 12 presents the reconstructed images at iteration 5 for the $XCAT_1$ and $XCAT_2$ phantoms at these scanner-specific acquisition times. Also here, the fifth iteration presents a good trade-off between noise and contrast. The detected true count rates for the different systems and phantoms are included as well. Based on visual assessment, the image quality in the torso region is similar between the different systems, especially in the coronal slices. However, the sagittal and transverse slices reveal elongation artifacts in the direction towards the detector panels, indicated by black arrows. The general anatomy and differences in uptake are preserved, but for instance in the brain, some contrast losses are observed. To quantitatively assess image noise, Figure 13 shows the standard deviation-to-mean ratio (noise in %) for 13 mm spherical ROIs placed in the lung, liver, and leg regions of both phantoms at iteration 5. For both XCATs, the noise in the lung and liver is similar for all three systems (at the selected scan times), whereas the noise in the legs is significantly higher for the ST-PET.

10.3389/fphy.2025.1712273

TABLE 2 Left: measured FWHM values (in mm) for the ST-PET system at different point source positions. Right: illustration of the different point source positions, and scanner axes.

Position	*x* (mm)	*y* (mm)	*z* (mm)	
Central	1.32	2.69	1.69	
10 cm radial	1.43	2.90	1.69	
40 cm axial	1.16	4.03	1.38	

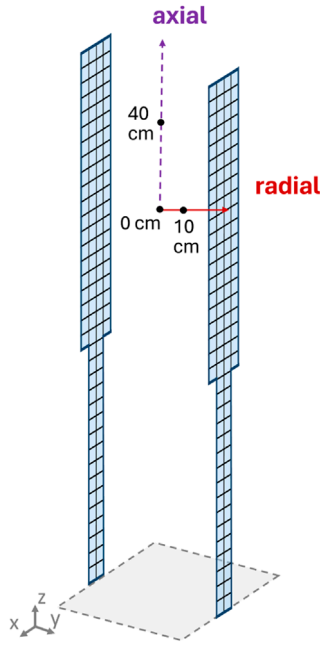

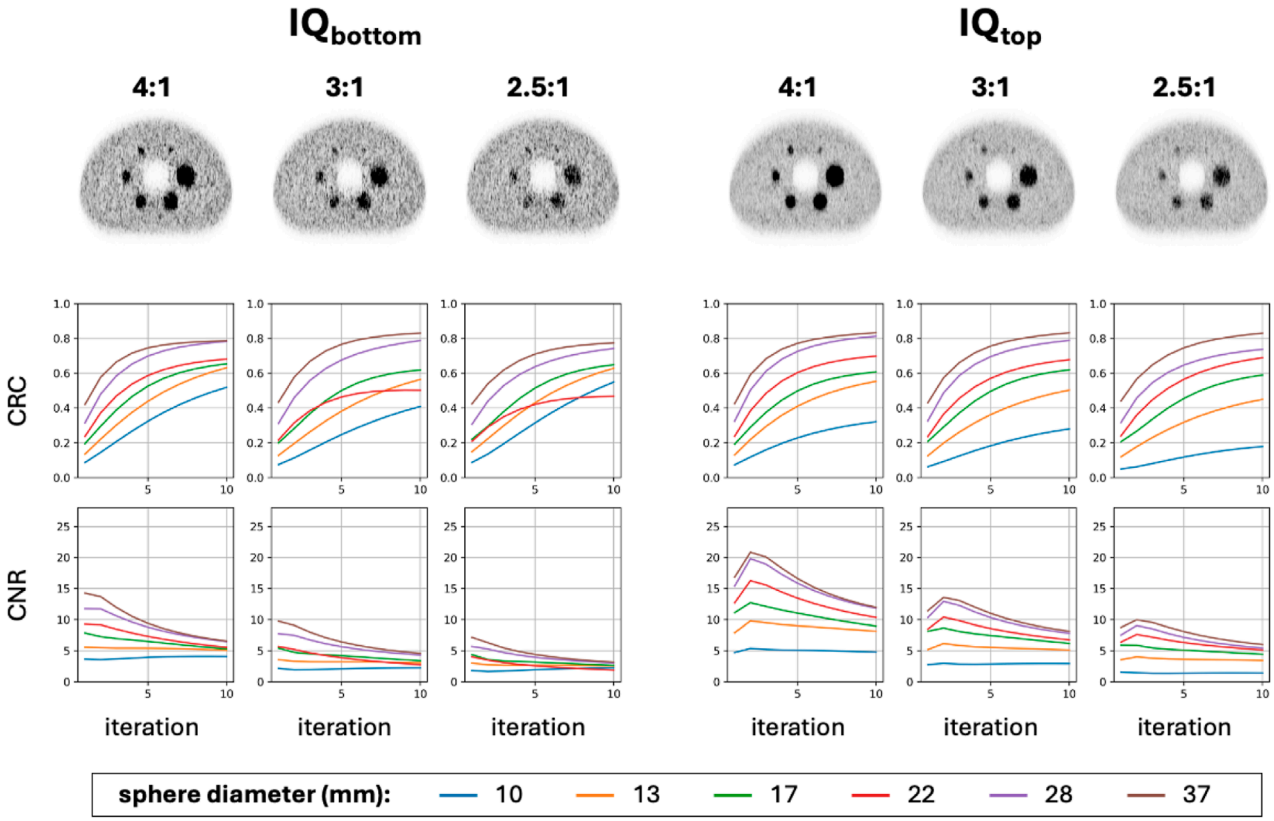

FIGURE 10
Transverse slices (fifth iteration) of the IQ phantom for source-to-background ratios of 4:1, 3:1 and 2.5:1. For the 4:1 acquisitions, the count rates in the bottom and top position were 7.63 and 2.03 million counts per minute respectively. Contrast-to-noise ratios (CNRs), and contrast recovery coefficients (CRCs) were calculated for iterations 1–10 to quantify image quality. All results are based on 4-min scans.

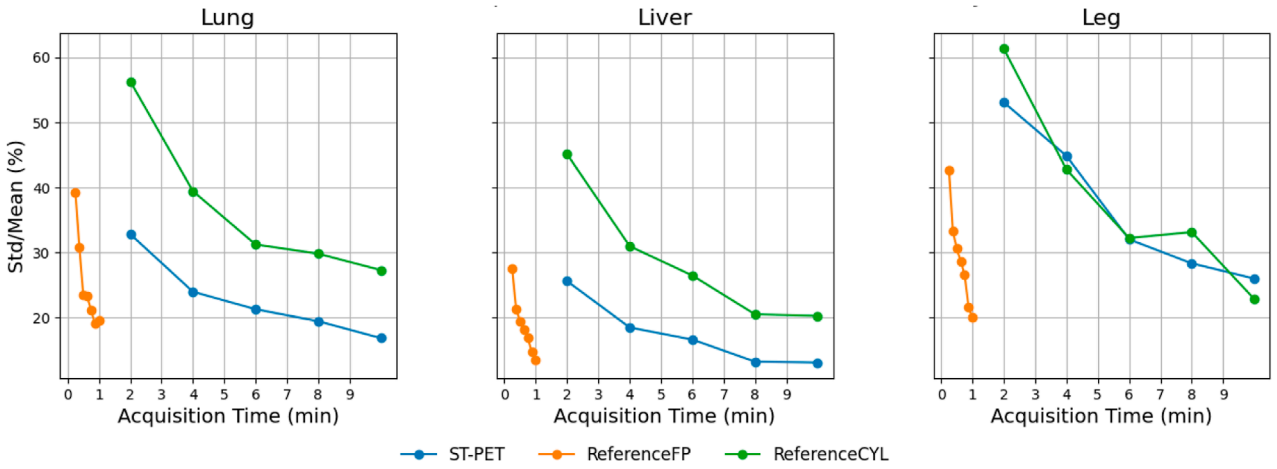

FIGURE 11
Standard deviation-to-mean ratio for 13-mm-diameter spherical ROIs in the lung, liver, and leg of $XCAT_1$ with normal BMI for varying acquisition times. ST-PET: blue, ReferenceFP: orange, ReferenceCYL: green.

4 Discussion

The panel motion study demonstrated the trade-off between focusing the sensitivity at the most relevant positions in the FOV and data completeness; while the parallel motion ensures broader anatomical coverage, it results in relatively low detection efficiency within relevant body regions. In contrast, the opposite panel motion enhances detection rates in the central torso but does not detect anything in peripheral regions such as the arms. The single-panel motion seems to offer a middle ground, but directs a large part of the sensitivity on one side of the panels, resulting in a low sensitivity on the opposite side. Therefore, the parallel motion seems the most relevant strategy for whole-body scanning of standard adults, since it provides uniform and broad coverage, even though it results in a somewhat reduced detection efficiency inside of the patient compared to the other two strategies. The results indicate that the motion strategy can however be tailored to the clinical application, potentially through hybrid or adaptive schemes, without drastically increasing system complexity.

Sensitivity measurements showed good agreement between the reference cylindrical system and the Biograph Vision 600 system, validating our simulation framework. The fact that the sensitivity of the ReferenceCYL system is about 20% lower than that of the Biograph Vision 600 can be ascribed to differences in detector characteristics, since the later features 20-mm-thick LSO detectors which have a slightly higher probability of stopping the gammas than the 16-mm-thich LYSO detectors of the ReferenceCYL system. Measurements confirm that ST-PET offers superior overall sensitivity compared to the cylindrical reference system, mainly due to placing the detectors closer together (50 cm vs. 80 cm), which results in higher geometric coverage for the same number of detectors. The differences in sensitivity between the flat-panel systems are explained by differences in panel width; whereas the ReferenceFP system spans an acceptance angle of 55.9°, the narrow top and bottom panels of the ST-PET only cover 22.7° and 11.6° respectively. Analogously, the ST-PET shows higher sensitivity in the torso region than in the legs for a 190 cm long cylindrical water phantom. The axial sensitivity profile confirms a uniform sensitivity profile for the cylindrical reference system and a nonhomogeneous sensitivity profile for the ST-PET system, showing increased sensitivity in the torso region and reduced sensitivity in the leg region relative to the cylindrical reference system.

The regional variation in sensitivity of the flat-panel ST-PET system directly influences image quality, as evidenced by both NEMA IQ and XCAT phantom results. Due to these differences in sensitivity, more noise is observed in the bottom than top regions. This is clearly illustrated by the differences in image quality between the two IQ positions. The top region showed higher CNR across all spheres and superior CRC values for the largest spheres. Based on ROI analyses in the XCAT phanom, it was shown that short 4-min scans in the ST-PET achieved acceptable image quality in the torso, while the reference cylindrical system required longer acquisitions (9.15 min) to reduce noise to similar levels. This finding supports the clinical feasibility of the ST-PET system, which aims for high-throughput scanning in an upright position, which might be uncomfortable to hold for extended periods of time. It is worth noting that noise levels in the legs were comparable between the ST-PET and ReferenceCYL for equivalent scan times, indicating the ST-PET's inherently lower sensitivity in the lower body and manifesting as increased noise with shorter scans. The ReferenceFP system supports even faster throughput, but would result in a restrictively high system cost.

As apparent from the sinograms in the panel motion study, both the ST-PET and ReferenceFP system do not provide full angular coverage. The missing projections are oriented parallel to the panels and result in elongation image artifacts towards the panels, both for the IQ and XCAT phantoms. While the limited angle artifacts in the XCAT images were somewhat more noticeable for the ST-PET than the ReferenceFP system, the difference is not as large as one might expect based on the transverse acceptance angles and sinogram masks. This discrepancy can be explained by the fact that both systems have the same large axial acceptance of

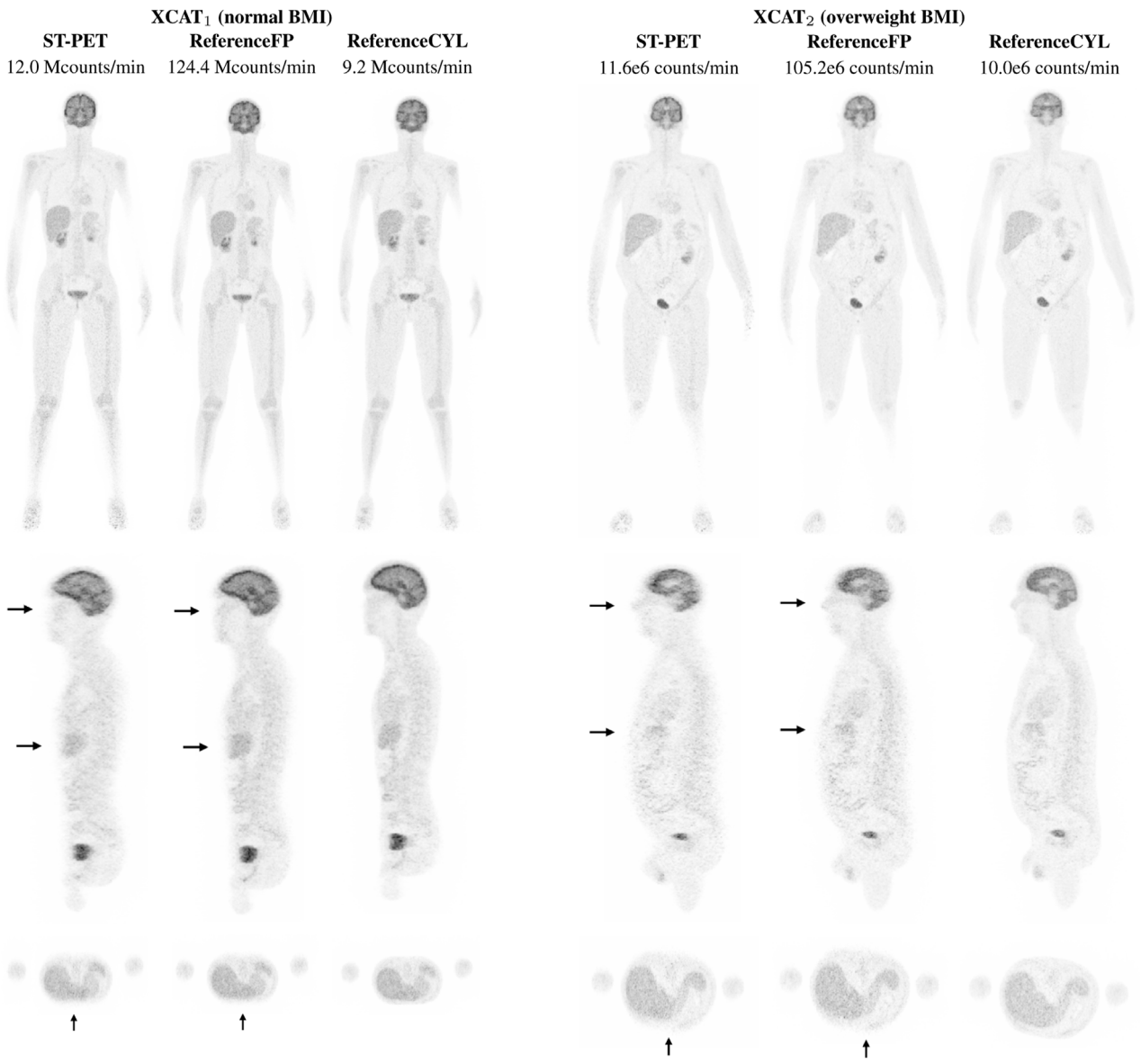

FIGURE 12
Reconstructed $XCAT_1$ and $XCAT_2$ slices at iteration 5 for the three PET systems with their respective acquisition times: ST-PET - 4 min, ReferenceFP - 30 s, ReferenceCYL-9.15 min. Detected count rates are indicated for in million (M) counts per minute. Black arrows indicate some regions where elongation artifacts, directed toward the detector panels, are most clearly visible, although they are present throughout the sagittal and transverse images.

75.3° which means that most information is actually sampled in the axial and not transverse direction–as opposed to the SAFOV cylindrical system. Additionally, the inclusion of TOF information relaxes the requirements on full angular sampling, and might help to equalize the presence of artifacts between different system widths. A similar observation holds true for the IQ images: while the quality of the image in the top panel is superior compared to that in the bottom panel, the main difference is caused by differences in noise (due to differences in sensitivity), rather than differences in angular sampling. While artifacts are noticeable in both the XCAT and IQ images, they do not interfere with overall visualization of structures with different uptakes, and all lesions of the IQ are well discernible. Further reduction of artifacts would require the development of detectors that provide a TOF resolution lower than the used 300 ps. Alternatively, advanced (DL-based) image processing tools have been proposed that help restore the original object boundaries after or during reconstruction [27, 28].

Despite the limited angle artifacts observed in the phantom images, the spatial resolution performance was excellent (<3 mm in all directions) at central positions, though some degradation occurred at large axial offsets. This aligns with previous observations, which showed that limited angle artifacts manifest more strongly for objects with a larger size [29]. The nonuniform behavior throughout the FOV stems from the system geometry and LOR characteristics,

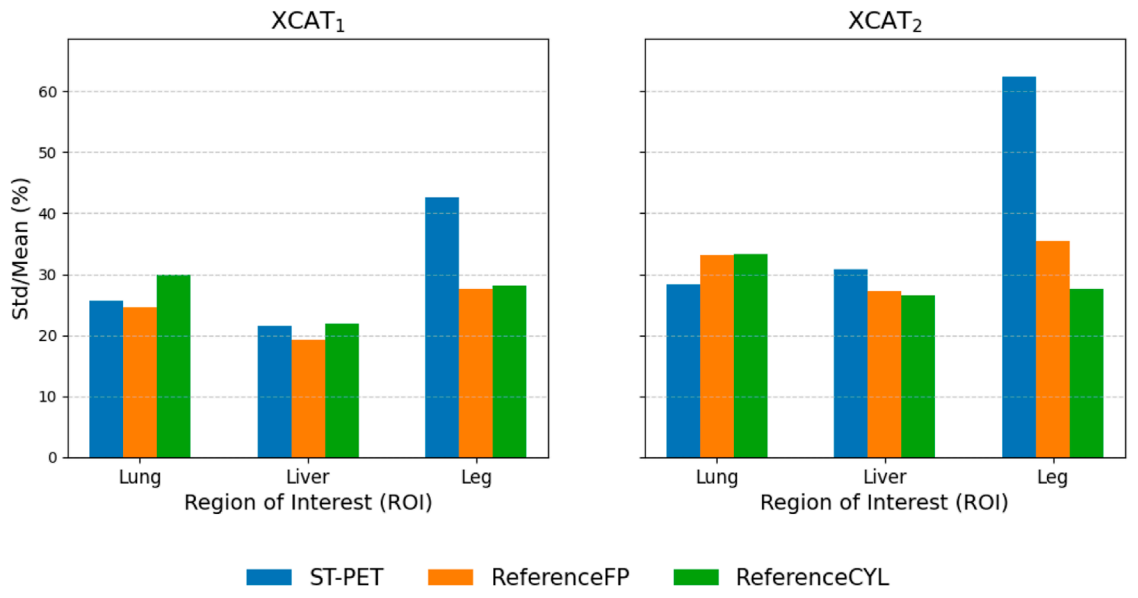

FIGURE 13
Standard deviation-to-mean ratio for 13-mm-diameter spherical ROIs in the lung, liver, and leg. Bars are grouped per ROI by PET system. Left panel: $XCAT_1$ (normal BMI). Right panel: $XCAT_2$ (overweight BMI). Data correspond to iteration 5. Scan durations: ST-PET (4 min), ReferenceFP (30 s), ReferenceCYL (9.15 min). ST-PET: blue, ReferenceFP: orange, ReferenceCYL: green.

where less oblique LORs at the axial offset position improves in-plane resolution but worsens resolution perpendicular to the panels due to further limitation of the angular coverage. Compared to conventional systems based on pixelated detectors arranged in a cylindrical geometry, the ST-PET achieves superior resolution due to its high-resolution monolithic detectors and DOI capability, though some degradation due to parallax errors and limited angle artifacts remains.

Previous studies by our group already highlighted the potential of upright flat-panel designs for high-throughput and cost-efficient PET imaging, since such geometries support fast and autonomous patient positioning and maximize the sensitivity for a given number of detectors. The original Walk-Through PET design features an AFOV of 106 cm and consists of two panels, comprising 14x20 detectors each (560 in total) [11]. Using simulations, we showed that this design provided competitive performance with the Biograph Vision Quadra (despite the presence of limited-angle artifacts), at only half or a third of the cost (depending on the used scintillation material, respectively LYSO and BGO) [10] As such, the system was presented as a promising entry-level LAFOV PET system. Compared to SAFOV systems, the WT-PET provides a significant performance improvement, while the cost is only 1.5–2 times higher (compared to a factor of 4 for the Quadra). Other, more high-end LAFOV PET systems are available on the commercial market, such as the uEXPLORER (AFOV of 2 m) [1]. These then offer additional sensitivity and image quality gains, but come with a significantly higher cost, scaling linearly with the length of the system, and are limited in throughput by the need for bed positioning.

Given the positive results of the WT-PET system simulations, variations on the design were devised for other imaging scenarios and applications. In another study, a low-cost variation of the WT-PET design was simulated, in which the AFOV was reduced to 60 cm and axial sparsity was introduced (with gaps of 28 cm), resulting in two panels of 12x8 detectors each (192 detectors in total). This system provided good performance at a component cost that was 30% lower than that of the Biograph Vision 600. Despite requiring limited axial translation for whole-body coverage, it maintained a higher patient throughput than current SAFOV and LAFOV systems [19]. These developments directly motivated the ST-PET design, which aims to cover the entire length of the patient in a cost-efficient way. This was obtained by reducing the width of the panels in two stages, achieving a 190-cm-long axial coverage using just 224 detectors. In this study, we showed that even such a very narrow design is capable of obtaining good image quality in relatively short scan times, and only mild limited-angle artifacts (comparable to those of the WT-PET configurations) were observed thanks to the very oblique LORs measured in the axial direction. As such, the system is proposed as a cost-effective, high-throughput solution for whole-body imaging, allowing for significantly lower scan times compared to conventional SAFOV PET systems at a slightly reduced component cost.

In summary, the ST-PET system combines high resolution imaging with high patient throughput, and its motion flexibility could be used for optimizing specific imaging protocols. Nonetheless, flat-panel architectures impose inherent limitations that challenge completely artifact-free whole-body imaging. Future efforts should focus on adaptive acquisition and reconstruction techniques to address these limitations, potentially enabling flat-panel PET systems to serve as cost-efficient alternatives for targeted clinical applications. Improved TOF performance would further enhance the capabilities of ST-PET, given its potential to further reduce limited angle artifacts.

5 Conclusion

The proposed ST-PET system demonstrates competitive performance, achieving sub-3 mm spatial resolution using monolithic detectors while enabling clinically feasible 4-min scans. Sensitivity measurements confirm that ST-PET offers superior overall sensitivity compared to the cylindrical reference system, with notably higher sensitivity in the torso region (1.66 cps/kBq) than in the legs (0.52 cps/kBq) for a 190 cm long cylindrical water phantom. Although challenges such as limited-angle artifacts and regional sensitivity variations persist, the system's cost efficiency and upright patient positioning provide distinct advantages over conventional SAFOV PET designs. These results support flat-panel PET as a viable alternative, especially for applications emphasizing high spatial resolution and improved patient throughput. Whereas the images suffer from limited angle artifacts with current TOF resolutions, expected future advancements in timing performance will further improve the image quality and thus relevance of the concept.

Data availability statement

The raw data supporting the conclusions of this article will be made available by the authors, without undue reservation.

Author contributions

ED: Data curation, Formal Analysis, Investigation, Software, Visualization, Writing – original draft. BV: Investigation, Methodology, Supervision, Visualization, Writing – review and editing, Formal Analysis. MA: Methodology, Software, Supervision, Writing – review and editing. JM: Software, Writing – review and editing, Resources. CV: Project administration, Writing – review and editing. SV: Conceptualization, Project administration, Writing – review and editing.

Funding

The authors declare that financial support was received for the research and/or publication of this article. BV acknowledges the support of a personal grant from Research Foundation Flanders (FWO), file number 1195125N.

Conflict of interest

The authors declare that the research was conducted in the absence of any commercial or financial relationships that could be construed as a potential conflict of interest.

Generative AI statement

The authors declare that no Generative AI was used in the creation of this manuscript.

Any alternative text (alt text) provided alongside figures in this article has been generated by Frontiers with the support of artificial intelligence and reasonable efforts have been made to ensure accuracy, including review by the authors wherever possible. If you identify any issues, please contact us.

Publisher's note

All claims expressed in this article are solely those of the authors and do not necessarily represent those of their affiliated organizations, or those of the publisher, the editors and the reviewers. Any product that may be evaluated in this article, or claim that may be made by its manufacturer, is not guaranteed or endorsed by the publisher.

Supplementary material

The Supplementary Material for this article can be found online at: https://www.frontiersin.org/articles/10.3389/fphy.2025.1712273/full#supplementary-material

References

1. Spencer B, Berg E, Schmall J, Omidvari N, Leung E, Abdelhafez Y, et al. Performance evaluation of the uexplorer total-body pet/ct scanner based on nema nu 2-2018 with additional tests to characterize pet scanners with a long axial field of view. *J Nucl Med* (2021) 62:861–70. doi:10.2967/jnumed.120.250597

2. Prenosil G, Sari H, Fürstner M, Afshar-Oromieh A, Shi K, Rominger A, et al. Performance characteristics of the biograph vision quadra pet/ct system with a long axial field of view using the nema nu 2-2018 standard. *J Nucl Med* (2022) 63:476–84. doi:10.2967/jnumed.121.261972

3. Dai B, Daube-Witherspoon M, McDonald S, Werner M, Parma M, Geagan M, et al. Performance evaluation of the pennpet explorer with expanded axial coverage. *Phys Med and Biol* (2023) 68:095007. doi:10.1088/1361-6560/acc722

4. Yamagishi S, Miwa K, Kamitaki S, Anraku K, Sato S, Yamao T, et al. Performance characteristics of a new-generation digital bismuth germanium oxide pet/ct system, omni legend 32, according to nema nu 2-2018 standards. *J Nucl Med* (2023) 64:1990–1997. doi:10.2967/jnumed.123.266140

5. Zhang H, Ren C, Liu Y, Yan X, Liu M, Hao Z, et al. Performance characteristics of a new generation 148-cm axial field-of-view umi panorama gs pet/ct system with extended nema nu 2-2018 and earl standards. *J Nucl Med* (2024) 65:1974–82. doi:10.2967/jnumed.124.267963

6. Vandenberghe S, Moskal P, Karp J. State of the art in total body pet. *EJNMMI Phys* (2020) 7:35. doi:10.1186/s40658-020-00290-2

7. Daube-Witherspoon M, Pantel A, Pryma D, Karp J. Total-body pet: a new paradigm for molecular imaging. *Br J Radiol* (2022) 95:20220357. doi:10.1259/bjr.20220357

8. Advanced Molecular Imaging Laboratory. Research: next-generation total-body tof-pet/ct with doi capabilities (2025). Available online at: https://pengqy-lab.szbl.ac.cn/reseach/(Accessed September 17, 2025).

9. Sanchez D, Jimenez-Serrano S, Laing A, Anreus A, Alamo J, Cañizares G, et al. Imas: a full-body pet system with enhanced tof and doi capabilities. In: *2024 IEEE nuclear science symposium (NSS), medical imaging conference (MIC)*

and room temperature semiconductor detector conference (RTSD) (2024). 1–2. doi:10.1109/NSS/MIC/RTSD57108.2024.10656775

10. Dadgar M, Maebe J, Abi Akl M, Vervenne B, Vandenberghe S. A simulation study of the system characteristics for a long axial fov pet design based on monolithic bgo flat panels compared with a pixelated lso cylindrical design. *EJNMMI Phys* (2023) 10:75. doi:10.1186/s40658-023-00593-0

11. Vandenberghe S, Muller F, Withofs N, Dadgar M, Maebe J, Vervenne B, et al. Walk-through flat panel total-body pet: a patient-centered design for high throughput imaging at lower cost using doi-capable high-resolution monolithic detectors. *Eur J Nucl Med Mol Imaging* (2023) 50:3558–3571. doi:10.1007/s00259-023-06341-x

12. Vandenberghe S, Daube-Witherspoon M, Lewitt R, Karp J. Fast reconstruction of 3d time-of-flight pet data by axial rebinning and transverse mashing. *Phys Med and Biol* (2006) 51:1603–21. doi:10.1088/0031-9155/51/6/017

13. Surti S, Karp J. Design considerations for a limited angle, dedicated breast, tof pet scanner. *Phys Med and Biol* (2008) 53:2911–21. doi:10.1088/0031-9155/53/11/010

14. Razdevšek G, El Fakhri G, Marin T, Dolenec R, Orehar M, Chemli Y, et al. Flexible and modular pet: evaluating the potential of tof-doi panel detectors. *Med Phys* (2025) 52:2845–2860. doi:10.1002/mp.17741

15. National Electrical Manufacturers Association. Nema standards publication nu 2-2018: performance measurements of positron emission tomographs (pets) (2018). Available online at: https://www.nema.org/docs/default-source/standards-document-library/nema-nu-2-2018-contents-and-scope.pdf?sfvrsn=1238765f_1 (Accessed November 03, 2025).

16. Sarrut D, Arbor N, Baudier T, Borys D, Etxebeste A, Fuchs H, et al. The opengate ecosystem for monte carlo simulation in medical physics. *Phys Med and Biol* (2022) 67:184001. doi:10.1088/1361-6560/ac8c83

17. van Sluis J, de Jong J, Schaar J, Noordzij W, van Snick P, Dierckx R, et al. Performance characteristics of the digital biograph vision pet/ct system. *J Nucl Med* (2019) 60:1031–1036. doi:10.2967/jnumed.118.215418

18. Stockhoff M, Decuyper M, Van Holen R, Vandenberghe S. High-resolution monolithic lyso detector with 6-layer depth-of-interaction for clinical pet. *Phys Med and Biol* (2021) 66:155014. doi:10.1088/1361-6560/ac1459

19. Abi Akl M, Maebe J, Vervenne B, Bouhali O, Vanhove C, Vandenberghe S. Performance evaluation of a medium axial field-of-view sparse pet system based on flat panels of monolithic lyso detectors: a simulation study. *EJNMMI Phys* (2025) 12:49. doi:10.1186/s40658-025-00766-z

20. Borghi G, Tabacchini V, Schaart D. Towards monolithic scintillator based tof-pet systems: practical methods for detector calibration and operation. *Phys Med and Biol* (2016) 61:4904–28. doi:10.1088/0031-9155/61/13/4904

21. Lamprou E, Gonzalez A, Sanchez F, Benlloch J. Exploring tof capabilities of pet detector blocks based on large monolithic crystals and analog sipms. *Physica Med* (2020) 70:10–18. doi:10.1016/j.ejmp.2019.12.004

22. Carra P, Bisogni M, Ciarrocchi E, Morrocchi M, Sportelli G, Rosso V, et al. A neural network-based algorithm for simultaneous event positioning and timestamping in monolithic scintillators. *Phys Med and Biol* (2022) 67:135001. doi:10.1088/1361-6560/ac72f2

23. Bezanson J, Edelman A, Karpinski S, Shah V. Julia: a fresh approach to numerical computing. *SIAM Rev* (2017) 59:65–98. doi:10.1137/141000671

24. Maebe J. *Timing capabilities and image reconstruction for the walk-through PET: a large flat-panel PET system with monolithic detectors. Ph.D. thesis*. Ghent: Ghent University (2024). 103–12.

25. Gong K, Cherry S, Qi J. On the assessment of spatial resolution of pet systems with iterative image reconstruction. *Phys Med and Biol* (2016) 61:N193–N202. doi:10.1088/0031-9155/61/5/N193

26. Dias AH, Hansen AK, Munk OL, Gormsen LC. Normal values for 18f-fdg uptake in organs and tissues measured by dynamic whole body multiparametric fdg pet in 126 patients. *EJNMMI Research* (2022) 12:15. doi:10.1186/s13550-022-00884-0

27. Maebe J, Dadgar M, Vandenberghe S. Deep learning limited angle artefact correction in the walk-through total-body pet system. In: *IEEE nuclear science symposium (NSS), medical imaging conference (MIC) and room temperature semiconductor detector conference (RTSD)* (2024). p. 1. doi:10.1109/NSSMICRTSD49126.2023.10337931

28. Raj J, Millardet M, Krishnamoorthy S, Karp J, Surti S, Matej S. Recovery of the spatially-variant deformations in dual-panel pet reconstructions using deep-learning. *Phys Med and Biol* (2024) 69:055028. doi:10.1088/1361-6560/ad278e

29. Maebe J, Vervenne B, Vandenberghe S. The effect of depth-of-interaction and missing projection angles on spatial resolution and elongation effects in a dual-panel pet system. *Total-body PET 2024, Abstr* (2024). Available online at: http://hdl.handle.net/1854/LU-01JQ6Z5APPN47MPDJDNS4NQFZB.